Journal of Alloys and Compounds 1017 (2025) 179020

Contents lists available at ScienceDirect

Journal of Alloys and Compounds

journal homepage: www.elsevier.com/locate/jalcom

Resolving the pressure induced ‘self-insertion’ in skutterudite $CoSb_3$

Bihan Wang [a,b], Anna Pakhomova [a,c], Saiana Khandarkhaeva [d], Mirtha Pillaca [e], Peter Gille [e], Zhe Ren [a,1], Dmitry Lapkin [a,2], Dameli Assalauova [a,3], Pavel Alexeev [a], Ilya Sergeev [a], Satishkumar Kulkarni [a], Tsu-Chien Weng [b], Michael Sprung [a], Hanns-Peter Liermann [a], Ivan A. Vartanyants [a], Konstantin Glazyrin [a,*]

[a] Deutsches Elektronen-Synchrotron DESY, Notkestr. 85, Hamburg 22607, Germany
[b] Center for Transformative Science, Shanghai Technical University, Shanghai, China
[c] European Synchrotron Radiation Facility, Avenue des Martyrs 71, Grenoble 38043, France
[d] Bayerisches Geoinstitut, University of Bayreuth, Universitätstr. 30, Bayreuth 95440, Germany
[e] Ludwig-Maximilians-Universität München, Department of Earth and Environmental Sciences, Crystallography Section, Luisenstr. 37, München 80333, Germany

ARTICLE INFO

Keywords:
Skutterudites
High pressure
Diamond anvil cell
Single crystal diffraction
Bragg coherent diffractive imaging

ABSTRACT

$CoSb_3$ belongs to the skutterudite family of compounds and serves as a crucial platform for the exploration of thermoelectric materials, however, its importance is equally high for studies of strong correlations at high pressures. Under compression it undergoes a ‘self-insertion’ isostructural transition resulting in a peculiar redistribution of large Sb atoms between different crystallographic sites. We conducted a comprehensive investigation of the structural phase stability of $CoSb_3$ up to 70 GPa using single crystal samples characterized employing conventional single crystal X-ray diffraction and X-ray scattering focused on measuring Bragg peak at high resolution (including elements of Bragg Coherent Diffraction Imaging). We explore the compression behavior of $CoSb_3$ in three different pressure transmitting media (PTM) and address several important, but previously unexplored topics: the influence of various PTMs and nonhydrostatic stresses on the strongly correlated system of $CoSb_3$, including the ‘self-insertion’ crossover, the phase stability of $CoSb_3$, the compound’s polymorphism, its crystal chemistry, and its peculiar evolution under pressure at ambient temperature. Among other important observations, we track the population of Sb atoms within the dodecahedral sites of $CoSb_3$ on compression, during the process of ‘self-insertion’, and on decompression. We detect that ‘self-insertion’ may not only reduce the solid’s compressibility, but also make it negative. Finally, but not least, we report that the ‘self-insertion’ crossover is an important step preceding a previously unknown phase transformation from cubic $Im\bar{3}$ $CoSb_3$ into trigonal $R\bar{3}$ occurring above 40 GPa, and discuss the distinctive behavior of $CoSb_3$ phases and their structural frameworks.

1. Introduction

At ambient pressure, the compound $CoSb_3$ ($Im\bar{3}$, S.G. 204) is known as an exceptional testbed for materials with enhanced thermoelectric properties and, as such, it is unsurprising that it has attracted significant amount of attention [1–8]. Its electronic, transport and various other properties have been studied for decades with a focus on understanding the material in its pure form and its potential to be tailored, e.g. by means of chemical doping. Indeed, the number of publications focused on alloying $CoSb_3$ to improve the properties of the resulting compound is steadily increasing [9,10]. It was a logical progression to investigate the behavior of $CoSb_3$ utilizing the chemically unaltering pathway of compression. And, indeed, compression paved a novel way for benchmarking theoretical studies and inspiring new avenues for synthesis and property customization of $CoSb_3$ [11–13]. A literature review reveals that, despite significant experimental progress in understanding the

---

* Corresponding author.
E-mail address: konstantin.glazyrin@desy.de (K. Glazyrin).

[1] Current address: Institute of High Energy Physics, Chinese Academy of Sciences, 100049 Beijing, China

[2] Current address: Institute of Applied Physics, University of Tübingen, Auf der Morgenstelle 10, 72076 Tübingen, Germany

[3] Current address: Constructor University, Campus Ring 1, D-28759 Bremen, Germany

https://doi.org/10.1016/j.jallcom.2025.179020
Received 10 September 2024; Received in revised form 27 January 2025; Accepted 4 February 2025

behavior of $CoSb_3$ at ambient pressure, studies conducted at high pressure are relatively scarce [11,13–16]. The topics of pure $CoSb_3$ as a strongly correlated system and its crystal chemistry remain largely underexplored. This is particularly surprising given the growing number of papers focused on high-pressure synthesis aimed at enhancing thermoelectric properties [9,10,16,17]. We must admit that we only have limited information with respect to the fundamental properties of $CoSb_3$, such as its structure, as a function of pressure and temperature. In this single crystal X-ray diffraction study we work on revealing missing information and, in particular, address the notable phenomenon of 'self-insertion' occurring above 25 GPa, which is clearly under-characterized even at ambient temperature conditions.

The definition of 'self-insertion' is attributed to a distinctive isostructural phase transition reducing the bulk compressibility of $CoSb_3$, hypothesized to be a result of an intricate Sb redistribution between the 24 g and 2a Wyckoff sites of space group $Im\overline{3}$ [11]. It was ascribed to a random reorganization of Sb atoms forming the corner sharing octahedron network of $Im\overline{3}$ $CoSb_6$ into void dodecahedral 2a sites of the low-pressure phase. Not only 'self-insertion' changes the material's elastic properties, it should also affect its electronic properties [14] and the currently missing information on crystal chemistry can provide further evidence. Considering a broader perspective and a bigger family of skutterudites, the 'self-insertion' is not a unique feature which can be attributed only to $CoSb_3$. Indeed, Matsui et al. presented evidence of 'self-insertion' in $RhSb_3$ and $IrSb_3$ [15]. Apart from thermoelectric applications [13], the process of 'self-insertion' is a very special case of a highly interesting strongly correlated behavior, but there are inconsistencies preventing us from crafting a cohesive picture. For example, previous studies reporting 'self-insertion' (e.g. [11,15]) were done in methanol:ethanol mixtures used as a pressure medium (highly non-hydrostatic above 10–12 GPa) and provided only selective and incomplete structural information.

In our pursuit to explore the pressure-induced structural evolution of $CoSb_3$ and to unveil new pieces of a bigger puzzle, we studied $CoSb_3$ compressed in various pressure transmitting media (namely He, Ne, Ar). This led to an enhanced characterization of the material and revealed its sensitivity to undesirable stresses and strains. It is known that phase stability in strongly correlated systems can be very sensitive to the overall energy landscape that is complexified by experimentally-generated stress/strain conditions [18,19]. Within the data reported by Kraemer et al. [11] and Matsui et al. [15] (see also Chapter (Ch.) 1 of Supplementary [20]), we detected anomalies of compressibility above 10 GPa, and in our study we carefully approach the topics of the crossover starting pressure, its width and correlate our observations with 'self-insertion' at various experimental conditions. Along the similar lines and given the large size of the targeted crystallographic sites relevant for 'self-insertion' (e.g. the dodecahedral sites of the $Im\overline{3}$ phase), we also explored the ability for the pressure transmitting media (PTM) to penetrate and occupy the latter, as it could potentially affect the overall process and the compound's final state. While this aspect has not been addressed before, our analysis of conventional single crystal X-ray diffraction provides a definitive answer to this question. Using various PTMs enables the ability to explore the impact of undesirable stresses and strains in realistic experimental loadings, but it represents only one aspect of the general picture. In our studies we also varied sample size from bulk single crystals to much smaller sub-micron particles prepared by a focused ion beam (FIB) and studied by with X-ray diffraction at large sample-to-detector distances with elements of Bragg Coherent Diffraction Imaging (BCDI) [21–25].

Finally, in this work we present a refined and extended picture of the phase diagram of $CoSb_3$ to pressures up to ~70 GPa at ambient temperature. Previous works were done on powder material compressed in diamond anvil cells (DACs), thus, our results which show changes in the crystal structure of $CoSb_3$ in response to compression provide a new reference for future theoretical benchmarks involving disorder in the atoms' occupancies. Among other results, we indicate that the process of 'self-insertion' is an intermediate step in the compression induced transformation of $CoSb_3$, with a new phase transition $Im\overline{3} \rightarrow R\overline{3}$ starting at ~40 GPa, following a group-subgroup relationship and resulting in the full filling of the crystal's dodecahedral sites in a contrast to a partial filling in the 'self-insertion' pressure range. Below, we present the study's experimental details and then discuss our observations on the peculiar evolution of the structure of $CoSb_3$ and its framework's building blocks under pressure. Here, we present very important and previously unknown details that adds to the broader understanding of this material beyond its thermoelectric properties.

2. Experimental

The $CoSb_3$ crystals were from the same batch as those used in our previous studies [26,27]. The crystals were grown using the inclined rotary Bridgman method from Sb-rich solutions [27]. The structure of material at ambient conditions is shown in Ch. 2 of Supplementary [20]. For conventional single crystal X-ray diffraction (CSC), we selected small shards broken from bigger crystals. Typically, the size of the shards did not exceed $30 \times 15 \times 5$ μm^3 to ensure the highest quasi-hydrostaticity, without sacrificing the signal-to-noise ratio. Hereafter, the last dimension corresponds to the thickness, and we will refer to these crystals as bulk crystals or CSC crystals.

Symmetric diamond anvil cells equipped with Boehler-Almax diamond anvils [28] with ~56–58° of effective X-ray conical aperture were used for pressure generation. The sample chambers were prepared by indenting a 250 μm thick Re foil. The thickness of the indented gasket and the initial sample chamber hole drilled in the gaskets varied depending on the diamond anvils' culet size. For diamond anvils with a culet diameter of 300 μm, we used a gasket hole diameter of 150 μm and indented the gasket to a thickness between 35 and 60 μm while for diamond anvils with a culet diameter of 200 μm, these values were of 100 μm and 30–36 μm, respectively.

Submicron-sized samples for high-resolution single crystal X-ray diffraction (HSC) were prepared in a different way. We prepared these samples by using a FIB system located at the DESY NanoLab (Hamburg, Germany), following a procedure similar to the one described in reference [26]. The preparation started by first cutting a lamella with a size of $14 \times 10 \times 0.5$ μm^3. Then, we mounted the lamella to a 2 μm thick amorphous silicon substrate (aSiN, produced by Norcada™) and reduced its volume, but keeping cube-like single crystal particles ($0.5 \times 0.5 \times 0.5$ μm^3) at the corners of a substrate. A small rectangular piece of aSiN holding four $CoSb_3$ sub-micron particles was cut out from a bigger piece of aSiN membrane and transferred to a diamond anvil culet (additional details, including microphotographs can be found in Ch. 3 of Supplementary [20]). Prior to transfer of the samples on a diamond anvil, the support of the aSiN piece was lightly engraved to enable recognizing the sub-micron sample positions within the sample chamber using visible light microscopes. Unlike the situation with CSC, where the samples could be easily located by X-ray absorption, a small piece of tungsten was placed as a reference in the vicinity of the aSiN rectangular support carrying the samples to facilitate finding them. In the case of HSC, we used mini-BX90 type [29] DACs with an effective X-ray aperture of ~70°.

As we show below, these small samples, at least at ambient conditions, could also be characterized by BCDI. Still, the primary task for HSC was to create the most quasi-hydrostatic conditions for a single crystal, ensuring that the amount of pressure medium was substantially larger than the studied object. This is often not the case in most high-pressure studies, including our CSC.

Here, we studied the same material with three different PTM: He, Ne and Ar. Considering CSC, below we report the results obtained when loading the sample each of the three PTM. For our HSC loading with sub-micron crystals, we used Ne in order to reduce risk of diamond anvil failure. With respect to the latter, Ne is considered as better quasi-hydrostatic PTM than Ar, but safer for the diamonds than He.

In CSC and HSC we used ruby as a pressure marker [30]. Marker from the same batch was crosschecked with the X-ray diffraction signal from the Ne and Ar PTM [31,32] in CSC studies. Standard deviation of pressure estimation was calculated from pressure standard measured before and after the collection.

Our experiments conducted on larger single crystals enabled estimating the material's unit cell compressibility as well as compressibility of inter-atomic distances, the characterization of 'self-insertion' and the resulting Sb occupancy of *2a* sites as a function of compression and decompression. To our knowledge, this is a first of a kind single crystal study covering the pressure range below 70 GPa. Using sub-micron FIB milled crystals allowed us to explore in greater detail the starting pressures of 'self-insertion' and compare the obtained results with the data on bulk crystals. Indeed, within our 'top-to-bottom' preparation procedure, the resulting sub-micron sized sample allowed us to increase the volume ratio between the PTM and the sample in an attempt to reach the best quasi-hydrostatic conditions from experimental point of view. These samples were studied with single crystal X-ray diffraction at a large sample to detector distance (i.e. at high resolution).

At the same time, by taking advantage of working with a sub-micron sample, we also exploited the possibility to conduct BCDI. The technique is novel for the high-pressure community working with diamond anvil cells (e.g. having significant stresses and strains within the samples as well as in between the samples and its surroundings), and presents great potential for new insights. Below, we show and discuss an important example for the high-pressure community and provide new observations and a new reference for the emerging field employing BCDI at extreme conditions.

2.1. Conventional single-crystal X-ray diffraction

Conventional high-pressure single crystal X-ray diffraction was measured at P02.2, PETRA-III, DESY, Hamburg, Germany [33]. Diffraction data were collected at room temperature using the Perkin-Elmer XRD 1621 detector (200×200 μm^2 pixel size). The wavelength was varied from one dataset to another (i.e. 0.2907, 0.2952 or 0.2955 Å). The single-crystal step-scans were collected during a continuous rotation along a vertical axis ω of $\pm$ 28–29°, depending on the DACs' X-ray aperture, with a step varying within 0.5–1°, depending on the dataset. We also collected oscillation images covering $\pm$ 20° within a single frame. Examples of 2D oscillation patterns can be found in the Ch. 4 of Supplementary [20]. The 2D patterns were inspected and analyzed using the DIOPTAS software [34]. Indexing and intensity integration was performed using CRYSALIS PRO [35], and for the crystal structure solutions and refinements we employed JANA2006 and OLEX2 [36,37] with SHELX [38,39]. Inspection of 1D patterns integrated from 2D images using DIOPTAS was also conducted with JANA2006. During the preparation and the writing of the manuscript, we additionally used VESTA [40] and CRYSTALMAKER [41] for the purpose of structure visualization. Error bars for the unit lattice constant and other parameters were determined using the corresponding software packages or general statistical methods.

The information covering the crystal structure solution is presented within the tables of Supplementary [20]. In addition to the tables, in the Supplementary [20] we provide Crystallographic Information Files (CIFs). We note that the disorder on the atoms' occupancies associated with the 'self-insertion' resulted in a significant broadening of the diffraction peaks' profile and thus, after the crossover, the data signal-to-noise ratio was lower. The effect can be seen in the diffraction patterns shown in the Ch. 4 of Supplementary and should not be confused with other potential effects, e.g. crystal bridging between diamond anvils, etc. The reduction of the signal-to-noise ratio affected the fit quality and resulted in higher values of the crystallographic R-factors. Still, we consider that our analysis reflects the crystal's structural evolution under high pressure conditions, and that the major conclusions remain unaffected. Considering the pressure stability field of the $R\overline{3}$ phase discussed below, due to limited beamtime, we could only measure its crystal structure at 68.8(2) GPa. The data points collected between 41 and 70 GPa were recorded as 2D oscillation patterns, which provide reduced angular information (e.g. without any correlation between Bragg peak position vs DAC rotation angle). Given the large number of observations, this information was still sufficient to calculate the $R\overline{3}$ phase's unit cell parameters.

2.2. High resolution single crystal diffraction and BCDI

The diffraction patterns from sub-micron particles were recorded at the Coherence Application P10 beamline of PETRA-III. The geometry of the scattering in the horizontal plane is depicted in Fig. 1. We used a partially coherent 13.1 keV X-ray beam focused to approximately 1×1 μm^2 using Compound Refractive Lenses (CRL) as focusing optics. Prior to data collection, the sub-micron crystals enclosed within a DAC were aligned to the rotation center of the diffractometer, with the sample-to-detector distance fixed to 1.83 m and with sample-signal scattering in the horizontal plane. The data of a pre-aligned $Im\overline{3}$ $CoSb_3$ (013) Bragg peak were measured using EIGER X4M detector (75×75 μm^2 pixel size). The $Im\overline{3}$ (013) peak the most intense diffraction peak accessible through the DAC's opening, having in mind the employed X-ray energy 13.1 keV, at all pressures of the study. In addition, our simulations indicated a strong correlation between $Im\overline{3}$ (013) and the 'self-insertion' crossover making (013) a strong indicator of the starting pressure of the compound's crossover transformation. At each pressure point, including ambient, we collected a full snapshot of the $Im\overline{3}$ (013) Bragg peak's intensity by step scanning. At each rotation step $\Delta\theta$, the detector captured a 2D diffraction pattern. These patterns were later assembled into a 3D diffraction pattern corresponding to the intensity distribution in reciprocal space. A typical collection involved obtaining ~300 2D diffraction patterns within $\pm$ 1° range.

Ambient conditions real-space images were reconstructed from the 3D intensity distribution (see discussion below). The pyCXIM package [42] was used to process the iterative algorithm which consisted of a sequence of ER350 + HIO800 + RAAR2100 + DIF1100 (where the following abbreviations were used: Error-Reduction (ER), Hybrid Input-Output (HIO), Averaged Alternating Reflectors (RAAR), Difference Map (DIF)). At every iteration, modulus and support constrains were applied. The shrink-wrap algorithm [43] was also included with a threshold range of 0.08–0.11. The best reconstructions were considered to be those with minimum Fourier space error.

3. Results and discussion

We start our discussion presenting data on sensitivity of phase transitions to sample environment and polymorphism of $CoSb_3$ below 70 GPa. By means of single crystal X-ray diffraction we could track the diffraction signal and the related parameters with high accuracy and precision. Considering the initial $Im\overline{3}$ phase, we report that the Bragg peak width of the (013) reflection, is very sensitive to pressure. In Fig. 2 we show the compression-induced change of the (013) Bragg peak full width at a half maximum (FWHM) as a function of pressure for bulk and sub-micron crystals using Ne as the pressure medium. We note that although for the case of CSC we used all observable equivalent reflections contributing to our oscillation images, for HSC sub-micron crystals we had access to only one of them.

For all four sub-micron crystals loaded into a DAC, the $Im\overline{3}$ (013) peak's FWHM increases within the pressure range of 24.3(2) to 29.7(2) GPa. We attribute it to the start of the 'self-insertion' for this HSC loading and provide an additional illustration in Fig. 3. The significant broadening of the (013) peak profile, as projected to the d-spacing axis at pressures above 25 GPa, cannot be simply explained by an average

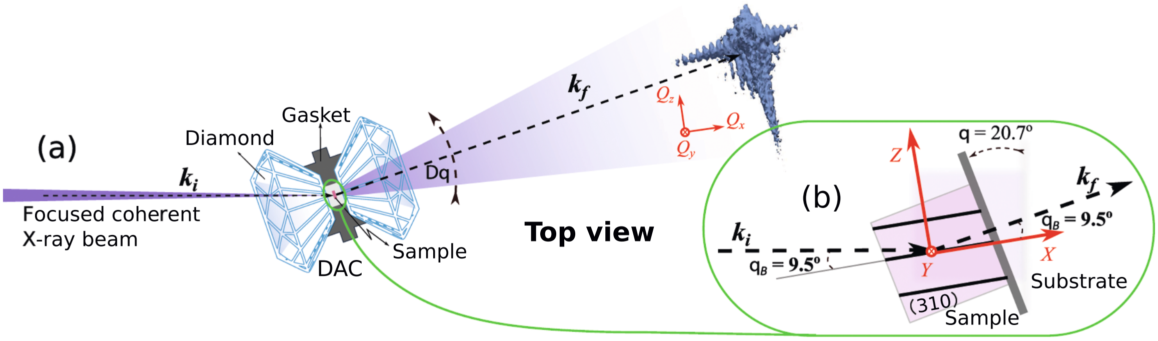

Fig. 1. Single crystal data collection geometry employed for sub-micron samples at the beamline P10, PETRA III. (a) Focused coherent X-ray beam illuminates the sample enclosed within the DAC. Data are collected by rotating the sample centered along θ axis in Δθ steps in order to extract the full $CoSb_3$ $Im\overline{3}$ (013) Bragg peak intensity. In (b) we show a sketch illustrating experimental geometry with the magnified sample mounted to the aSiN substrate.

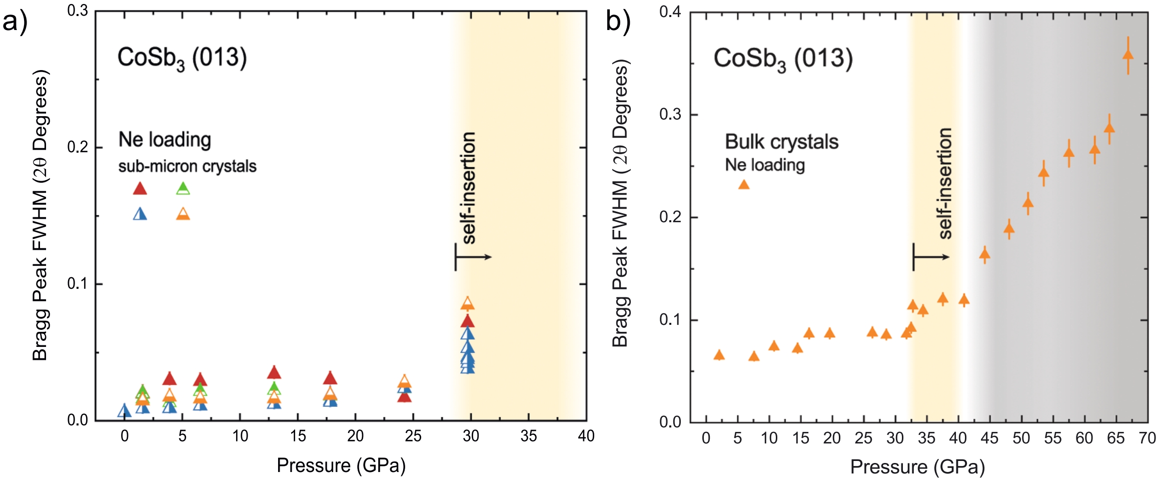

Fig. 2. Selected full width at half maximum (FWHM) data of Bragg peaks attributed to $Im\overline{3}$ $CoSb_3$ (013) at pressures below 40 GPa and its variation under compression. In panel (a) we show the results for sub-micron HSC crystals in Ne PTM collected at 13.1 keV at high resolution, while in (b) we show selected results from bulk CSS loaded using the same PTM and collected at 42.65 keV. Arrows indicate an apparent broadening of the Bragg peak coinciding with the process of 'self-insertion'. Considering four different sub-micron crystals mounted at the same substrate, we see a slight difference in their behavior (e.g. red, orange and blue symbols), but the result is consistent. We note that in (a) the transition happens at earlier pressures in comparison to the data shown in (b). Considering the pressure point of ~29 GPa shown in (a), different blue symbols indicate several different measurements at the same crystal. Finally, for (b) we report that at pressures exceeding 40 GPa, the equivalent reflections (attributed to (01_3) $Im\overline{3}$ $CoSb_3$ ambient pressure phase) become split indicating a phase transition. We use different shading to separate various pressure ranges. The error bars are indicated, if not visible, they are the size of symbols or below.

particle strain (bulk strain), as the asymmetry of the Bragg peak changes. Indeed, at lower pressures, we observe a small tail at higher d-spacing values, while at higher pressures we see a stronger broadening and asymmetry developing on the peak's opposite side.

Our HSC data are limited to ~30 GPa, but within the CSC data we can find additional evidence of the aforementioned 'self-insertion' onset. Indeed, the FWHM of the (013) reflection in a bulk crystal (CSC) loaded with Ne begins to broaden at a pressure of 32.4(2) GPa, thus, at higher pressure in comparison to HSC loaded with same PTM. As indicated using shading in Fig. 2b, the broadening of CSC reaches saturation below ~40.9(2) GPa. Further increase of the (013) FWHM is observed at higher pressures.

Considering the pressure range below 70 GPa, in contrast to Matsui et al. [15] (powder diffraction data, methanol-ethanol mixture as the PTM), instead of two distinct pressure regions we highlight three: (1) below the 'self-insertion' when the Sb population of the $Im\overline{3}$ 2*a* Wyckoff site is 0, (2) during the 'self-insertion' when the Sb occupancy of 2*a* Wyckoff sites becomes non-zero and (3) when the $Im\overline{3}$ phase of $CoSb_3$ is transformed via a group-subgroup relation into a lower symmetry structure. The latter conclusion is supported by our observation of the $Im\overline{3}$ (013) peak's splitting, described in greater detail in the Ch. 4 of Supplementary [20]. Analysis of our CSC data allows us to index the new structure as $R\overline{3}$ (S.G. 148) with twelve formula units per unit cell ($Z = 12$) in contrast to eight formula units for the $Im\overline{3}$ phase ($Z = 8$).

Before we come to the description of the material's compressibility and the $R\overline{3}$ structure, we clarify several important points. First of all, we note that our CSC data excludes any incorporation of He, Ne or Ar at the dodecahedral sites of the $CoSb_3$ polymorphs, as tested in multiple loadings and supported by our crystal structure refinements as well as by observations of the material's compressibility (discussed below). In addition, considering the Sb atoms' occupancy of the dodecahedral sites triggered by the 'self-insertion', we report that the measured values correlate with our observations of the (013) broadening, as we indicate in Fig. 4. Data shown in the figure support our conclusions on self-insertion's starting pressure for CSC samples. For the simplicity of the representation, we only show the experimental points close to the 'self-insertion' and skip the lower pressure points preceding the crossover. For the sake of completeness, we note that in order to fully fill the dodecahedral Wyckoff sites of the $Im\overline{3}$ unit cell, we require only two Sb vacancies, per unit cell, at the $Im\overline{3}$ 24 *g* Wyckoff sites (Sb forming octahedral arrangement around Co). The final Sb occupancy of the dodecahedral sites, prior to a full transition to the $R\overline{3}$ phase does not

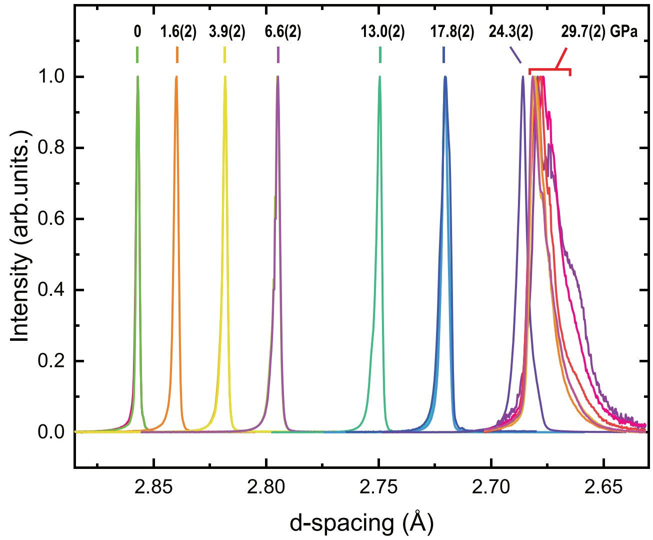

Fig. 3. Variation of $CoSb_3$ $Im\overline{3}$ (013) Bragg peak profile as projected to d-spacing axis. For a simplicity of presentation, we show data from a single sub-micron particle normalized to its maximum intensity. Upon compression, the width of the Bragg peak broadens. Below 24.3(2) GPa, the broadening is visible and could be attributed to the average strain of the particle. For pressure points above 24.3(2) GPa, collected at apparently the same pressure conditions, as indicated by the pressure sensor measured before and after the measurements at P10, we see significant broadening which cannot be exclusively attributed to the average particle stain. Profiles shown for 29.7(2) GPa correspond to several data sets collected on the same particle.

reach 100 %, indicating that the degree of 'self-insertion' is an important factor for the $Im\overline{3}\rightarrow R\overline{3}$ transformation. Finally, we note that decompression to ambient pressure of a CSC sample loaded in an Ar PTM shows a clear hysteresis with the final antimony occupancy at the dodecahedral sites reaching a value of 28(1)%.

Next, if we compare our data with literature, we see that the starting pressures of the 'self-insertion' of HSC samples compressed in Ne and CSC samples compressed in Ar and Ne pressure media differ from one another significantly. In all our loadings, the 'self-insertion' starts at values reproducibly higher than the values reported in the original publication of Kraemer et al. [11] and Matsui et al. [15]. It is also worth to note that in contrast to Kraemer et al. [11] and Matsui et al. [15] (powder material, methanol-ethanol mixture used as the PTM), our data reproducibly indicates that prior to the $Im\overline{3}\rightarrow R\overline{3}$ transition, the 'self--insertion' transition occurs over a relatively narrow pressure range.

In the following lines we discuss results of X-ray diffraction with a coherent beam and high resolution: investigation of sub-micron $CoSb_3$ particles at ambient and elevated pressures. Indeed, CSC under extreme conditions has advantages and limitations. In comparison to HSC, it has much lower detection limit of initial sample strain conditions. Investigations of X-ray diffraction under high resolution and the application of BCDI can help us shed light on the initial micro-strain conditions of the sub-micron samples. We consider that it is important to share these observations with the community because of several reasons. On one hand we want to attract the community's attention to the power and limitations of BCDI applied at high pressure. On the other hand, it is also one of the rare cases when a sample under extreme condition prepared using a 'top→bottom' approach in which a smaller particle was cut from a much larger crystal was analyzed by BCDI.

First of all, in Fig. 5 we show data for a submicron particle

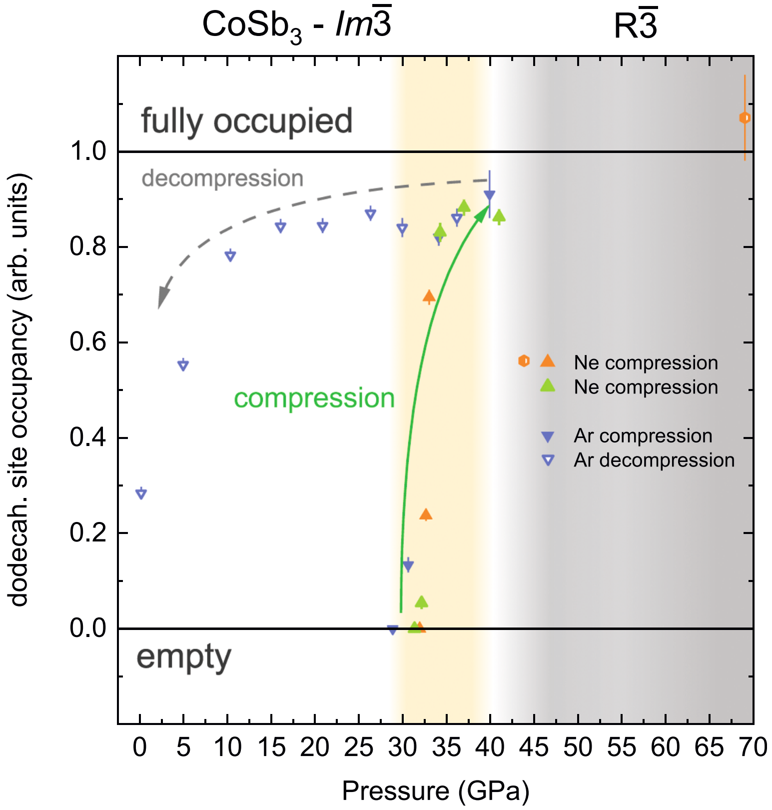

Fig. 4. Antimony occupancies of dodecahedral sites in $CoSb_3$ $Im\overline{3}$ and $R\overline{3}$. Different CSC sample loadings are indicated by symbols with different color. The open blue triangles indicate decompression of CSC in Ar PTM. The orange hexagon corresponds to $R\overline{3}$ structure. In order to show the error bars for the latter, we intentionally allowed the data analysis fitting procedure it to vary above the physically possible value of 1. Grey shading indicates the phase stability field of $R\overline{3}$ phase and yellow shading indicates 'self-insertion' crossover. The occupancy is shown as a dimensionless unit with 0 and 1 corresponding to 0 % and 100 %, respectively. Legend of the figure provides additional information on PTMs used in individual loadings.

transferred together with as aSiN support into a sample chamber of a DAC. The data were measured at ambient pressure and temperature prior to sample pressurization along with a PTM. The HSC 3D submicron particle shape and the strain component ε_{zz} with direction of Z along the scattering vector (013) of the $Im\bar{3}$ phase were determined by phase retrieval from the 3D diffraction pattern. The voxel size of our reconstruction given by the dimensions of probed reciprocal space was about 16 nm. The data shown in Fig. 5 represents a sum of 50 best results out of the 100 reconstructions. The reconstructed nanoparticle shape can be described as a cuboid with rounded corners, and edges with a characteristic edges side of ~ 540 nm. This value is in a good agreement with measurements conducted with the FIB dual beam machine. Our analysis resolves some strain at the surface of the nanoparticle, potentially induced by the preparation procedure of the FIB cutting. Still, these values are minimal in comparison to the more homogeneous central part. Based on our observations during this ‘top→bottom’ sample preparation approach for BCDI, we suggest that the concepts of sample pre-characterization, sample redundancy and experimental reproducibility become critical. Pre-characterization of multiple BCDI samples requires significant amount of beamtime which should be carefully considered by the high-pressure community.

Considering the compression of the same sample in Ne, the stress-induced changes in the diffraction signal are well seen in Fig. 6. After comparison of the intensity distribution for different pressure points, we detect significant variations between the recorded signals. We observe the effect of compression starting at a pressure as low as 1.6(2) GPa. The signal becomes more and more complicated with each further pressure step. The strong contrast change between the points of 24.3(2) GPa and 29.7(2) GPa contributes to our discussion of developing ‘self-insertion’. Notably, similar changes are observed for other measured particles mounted to the same aSiN substrate, as demonstrated in the Ch. 5 of Supplementary [20]. Unfortunately, the BCDI reconstruction of high-pressure data did not yield a reliable result for neither of the prepared ‘sub-micron’ particles subjected to high-pressure conditions in a Ne PTM.

Within our discussion we are ready to move on and describe compressibility and crystal chemistry and of CoSb$_3$ below 70 GPa. Evolution of the CoSb$_3$ unit cell volume normalized to the number of formula units (Z) in each compound is shown in Fig. 7. In previous publications of Kraemer et al. [11] and Matsui et al. [15], it has been suggested that the process of ‘self-insertion’ should be attributed to a rare phenomenon of reduced compressibility. Our data on two independent Ne loading (e.g. orange and green symbols) shows that the observation of negative compressibility, namely with the volume of the material’s unit cell increasing under compression, is also possible (see the pressure region between 30 and 35 GPa). The contrast between various observations, including the example of loading Ar PTM, requires some additional discussion.

In our work we describe multiple loadings of different sample size loaded with different PTMs. Considering Fig. 7, for pressures below the ‘self-insertion’ crossover, indicated using orange shading, we see a very good agreement between the CSC and the HSC data. Although the scatter of the data points between different quasi-hydrostatic loadings is minimal, we still observe a small mismatch in the volume-pressure data. For example, it is seen for two different Ne loadings at presumably similar degree of quasi-hydrostaticity and with samples of similar size (e.g. orange and green triangles). The contrast of the Ne PTM data with data corresponding to an Ar PTM loading is more significant. In order to explain different observations, we need to have in mind the stress components’ distribution complexity in a realistic DAC experiment, present even for samples with a small size [18]. In our study, we see that although having a single crystalline material may reduce effects of undesirable inter-grain strains, there are situations and systems particularly sensitive to even small deviations from ideal hydrostatic conditions (e.g. deviatoric stress, pressure gradients and systematic shift of a pressure marker reading with respect to the stresses at a sample). Our study shows that such effects could play a significant role also in situations when the studied crystals are not bridged by the diamond anvils. The factors mentioned here should be given due attention, and the case of the CoSb$_3$ shows that the effects can be very strong. Here, we note that although the degree of ‘self-insertion’ completeness is very close for the Ar and Ne loadings (see variation of occupancies as a function of pressure shown in Fig. 4), the recorded unit cell volumes corresponding to the ‘self-insertion’ differ significantly. Considering the data collected above 40 GPa, we understand that they could bear even stronger systematic shift due to some presence of undesirable stresses. At the same time, it is important to highlight that these results represent an important example and act as a reference, but do not change our conclusions.

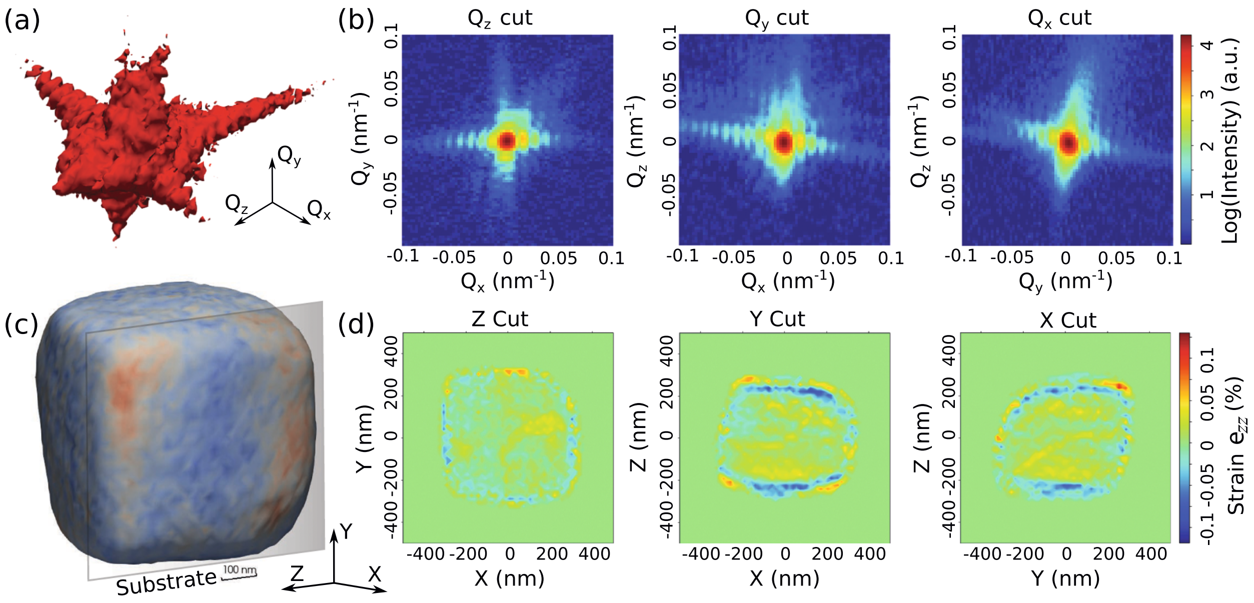

Fig. 5. BCDI analysis of a selected particle loaded in a DAC, mounted to an aSiN substrate at ambient conditions. (a) The 3D representation of the diffraction pattern. (b) The diffraction patterns cut through the center of mass of the intensity in Q_z, Q_y, Q_x. (c) The side view of the reconstructed nanoparticle with surface colored according to the strain field ε_{zz}. The aSiN substrate is shown as a transparent plane with respect to the particle. (d) Illustration of ε_{zz} strain represented by means of slices going through the center of nanoparticle mass. All diffraction patterns presented in (a, b) are shown on logarithmic scale.

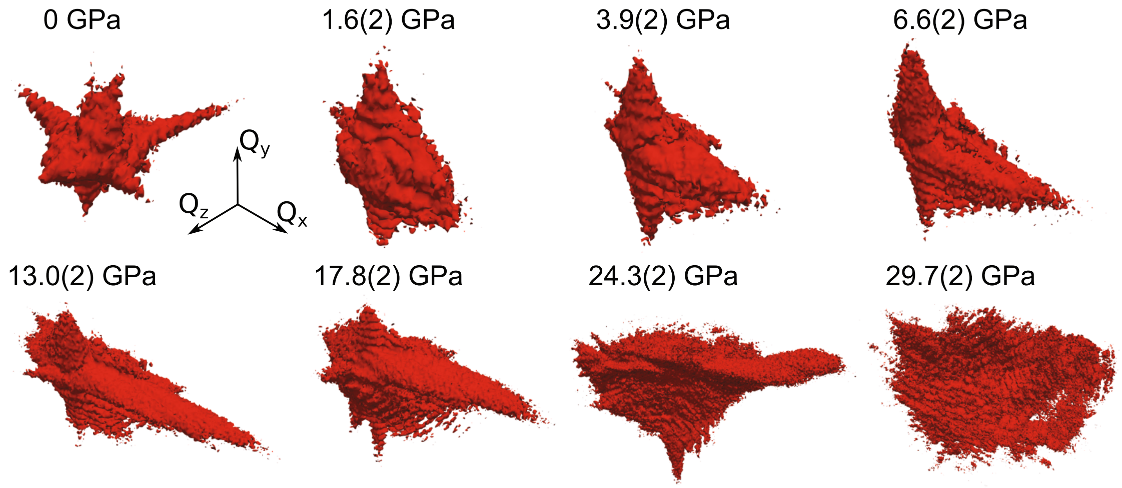

Fig. 6. Evolution of a selected CoSb$_3$ sub-micron particle $Im\bar{3}$ (013) Bragg peak signal as a function of pressure. This representation shares the similar intensity threshold as data shown in Fig. 5. The particle was compressed in Ne PTM. Even at pressures preceding the 'self-insertion' (e.g. below 29.7(2) GPa), we see a strong effect of compression on the particle signal. While the average strain on the particle is low, the effect of micro-strains accumulated with large pressure steps and at the starting pressure of 'self-insertion' (e.g. 29.7(2) GPa) is clearly visible. The shape becomes much more distorted in comparison to the 24.3(2) GPa point at higher pressure value.

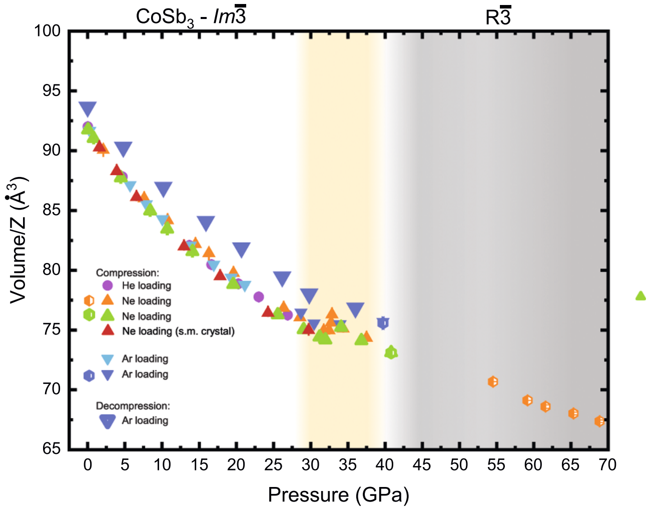

Fig. 7. Compressibility of CoSb$_3$ unit cell normalized to the number of formula units (Z) per unit cell as a function of pressure. Legend of the figure provides additional information on PTMs used in individual loadings. The region of 'self-insertion' highlighted using the orange shading. The phase stability of $R\bar{3}$ is indicated by grey shading. We note good agreement between data from CSC (loaded with various PTMs) and HSC sub-micron crystal. For simplicity of representation we show data for a single HSC particle. Signal for the other HSC particles can be considered as overlaid by the red triangle. Solid circles and triangles correspond to the cubic $Im\bar{3}$ phase. At the same time hexagons correspond to the trigonal $R\bar{3}$ phase. Open inverted triangles correspond to data collected on decompression in Ar PTM, during the same loading as indicated by solid blue triangles. For the reader's convenience, for the selected points at ~40 GPa we present unit cell volumes calculated for both $Im\bar{3}$ and $R\bar{3}$. Our data illustrates that even if the crystals are small and the pressure range is relatively low, there are discrepancies in volume vs pressure for various loadings even if we compare loadings with the same pressure medium. This observation suggests enhanced sensitivity of CoSb$_3$ to external environment. Orange symbols correlate with data shown in Fig. 2 and Fig. 4. If error bars are invisible, they are the size of the symbols or below.

The disorder of the atoms' occupancy attributed to a 'self-insertion' crossover has been lacking a thorough characterization if crystal chemistry is considered. The body-centered structure of the low-pressure cubic CoSb$_3$ phase has only two independent/general atomic coordinates which can be tuned as a function of pressure or temperature [44]. Both of them are attributed to the Sb1 24 *g* Wyckoff site with coordinates (0 Y$_{\mathrm{Sb1}}$ Z$_{\mathrm{Sb1}}$). Considering the evolution of Y$_{\mathrm{Sb}}$ and Z$_{\mathrm{Sb}}$ (Fig. 8), we detect a slight change at the beginning of the 'self-insertion' phenomenon (e.g. with the Ne and Ar PTMs). However, due to the unique

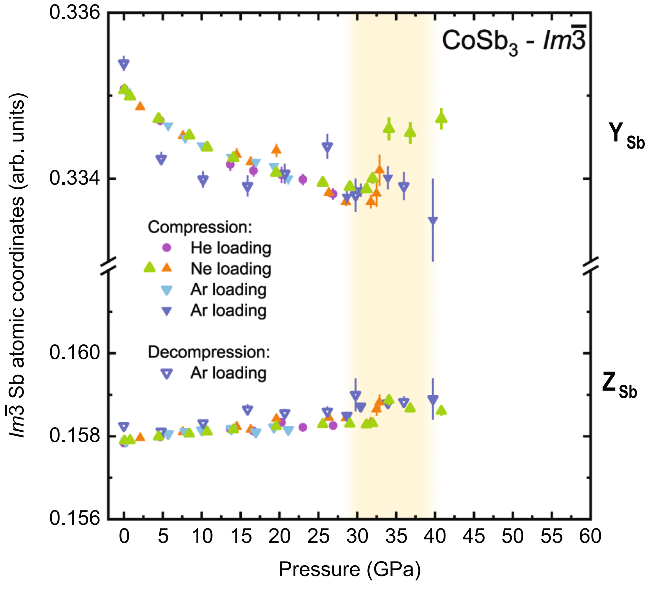

Fig. 8. Evolution of CoSb$_3$ $Im\bar{3}$ Sb atom coordinates as a function of pressure. Solid circles and triangles correspond to the cubic $Im\bar{3}$ phase. Legend of the figure provides additional information on PTMs used in individual loadings. We highlight the region of 'self-insertion' using the yellow shading. Open inverted triangles correspond to data collected on decompression in Ar PTM, i.e. during the same loading as indicated by solid blue triangles. Considering the compression in Ne, we start to see signs for anomalous behavior, namely increasing Y$_{\mathrm{Sb}}$ and Z$_{\mathrm{Sb}}$ at the early stages of 'self-insertion'. The deviation of data collected in Ar PTM on compression from data collected in Ne PTM could be attributed to the unit lattice mismatch for the given pressure range (see Fig. 7). Along similar lines, we should attribute the dynamic behavior of Y$_{\mathrm{Sb}}$ on decompression to the interplay of various factors, including larger volume of the material undergone 'self-insertion' in comparison to the preceding compression run.

stress conditions of the corresponding crystals, we observe a stronger contrast between samples in different PTM at higher pressure. Again, it could be attributed to the fact that Ar is considered to be a less quasi-hydrostatic pressure medium in comparison to Ne [45], but coupled with the enhanced susceptibility of $CoSb_3$ to external disturbances in the region of 'self-insertion'. We see that at pressures below ~35 GPa, the data collected on samples in Ar matches well with the data for samples in Ne. If we compare Fig. 4 with Fig. 8, we see that the 'self-insertion' is attributed to larger unit cell volume values for sample loaded with Ar in comparison to samples loaded with Ne. It should explain the difference between the atomic coordinate values measured for different pressure media within the crossover region, as well as the data on decompression collected from sample subjected pressurized in Ar. The evidence presented so far indicate that 'self-insertion' is very sensitive to the sample's surrounding environment and complexity of stress and strain distribution within it. We suggest that this conclusion should be generalized for a wide range of unfilled skutterudite systems (e.g. those of the $Im\overline{3}$ space group with an unfilled *2a* site), including the above mentioned $RhSb_3$ and $IrSb_3$. Potentially, it could also be applied to partially filled skutterudite systems.

The CSC data collected for $CoSb_3$ allows us to see variation in the atomic coordinates as well as Co-Sb and Sb-Sb distances under pressure, providing more insight and more information for future theoretical calculation which could explain strong correlations on the level of electronic interactions and bonding. The corresponding values are shown in Fig. 9. Upon the 'self-insertion', we observe an enhanced rigidity of Co-Sb distances forming $CoSb_6$ octahedra for loadings with an Ar PTM and even their expansion with an Ne PTM. Although, within the $Im\overline{3}$ phase all six Co-Sb distances attributed to the $CoSb_6$ octahedron are the same, we observe that within the $R\overline{3}$ phase their diversity increases, and that the resulting octahedra become more distorted in comparison to the cubic phase.

In comparison to Co-Sb atomic distances, the character of the shortest Sb-Sb distances does not change significantly, with the exception of the 'self-insertion' crossover region, where the compression induced trend seems to stiffen. At pressures above the crossover, the interatomic distances continue to decrease monotonously. The lowest values correspond to Sb-Sb bonds contributing to the shell of dodecahedral sites, while the second longer distances – to the distances interconnecting them (see also the Ch. 1 of Supplementary [20]). Considering the comparison with ambient pressure data, the distances shown in Fig. 9b are very close to the value of 2.908(1) Å for the Sb-Sb bond in pure antimony [46,47], with one Sb-Sb distance in $Im\overline{3}$ $CoSb_3$ being slightly larger and one slightly smaller. After the review of available literature [48–51], we suggest that the Sb-Sb bond for pure antimony decreases, but stays close to the values observed in our study. This raises the question regarding the distances between Sb atoms occupying the centers of dodecahedral sites, as a result of 'self-insertion', and their closest neighbors, which are other Sb atoms. The corresponding values are shown in Fig. 10.

While the electronic density of the large Sb atoms is highly compressible, we have no doubts that the distances shown in Fig. 10 exceed values attributed to the Sb-Sb bond in pure antimony under pressure [50,51]. Indeed, the process of 'self-insertion' forces a very rapid and coordinated isostructural atomic reconstruction over the bulk of the $CoSb_3$ $Im\overline{3}$ phase, moving the Sb atoms over a distance of ~3.1 Å, which is very significant if we consider atomic scale. To illustrate the magnitude, we note that the shortest distance between Na and Cl in rock salt is 2.8169(4) Å at ambient (e.g. an example of a system with large ionic radii [52]). Typical pressure induced reconstructions (e.g. of martensitic origin) are generally much smaller.

As a metalloid and unlike smaller pnictogens, Sb may not always require a strong covalent bond. Following the ab-initio analysis shown within the supplementary of reference [14], where the authors simulated the intrinsic disorder of 'self-insertion' by introducing an additional Sb atom in the dodecahedral site of $SbCo_4Sb_{12}$, we could support the hypothesis suggesting that the compounds produced by 'self-insertion' undergoes a change of the initial material electronic state. Data shown in Fig. 9 and Fig. 10 indicate that at 70 GPa, the distance between the dodecahedron central Sb atoms is still ~0.2 Å larger than the largest Sb-Sb bond distance for Sb atoms forming the dodecahedron shells and the interconnections between them. Moreover, it is likely that the valence state of Sb filling the dodecahedral sites as a result of 'self-insertion' is close to zero. We also suggest that the binding of the Sb

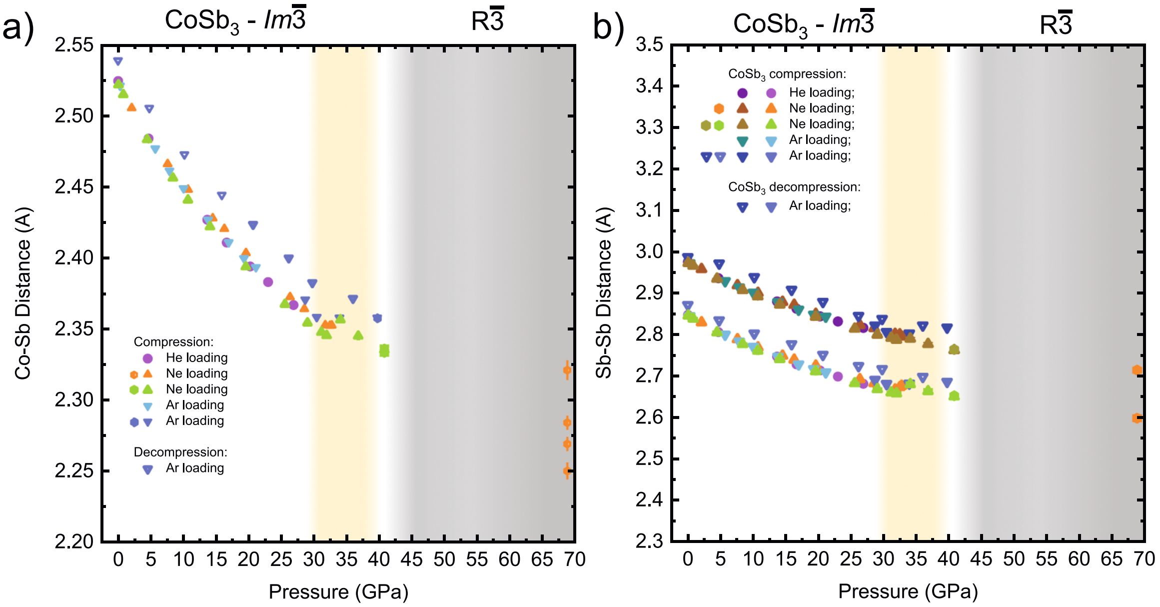

Fig. 9. Variation of shortest near-neighbor (a) Co-Sb and (b) Sb-Sb distances as a function of pressure. We indicate the region of the 'self-insertion' using the yellow shading and the stability field of $R\overline{3}$ using the gray shading, respectfully. The orange hexagons correspond to the trigonal $R\overline{3}$ phase. Open inverted triangles correspond to data collected on decompression in Ar PTM, i.e. during the same loading as indicated by solid blue triangles. For the reader's convenience, for the selected points at ~40 GPa we present values calculated for both $Im\overline{3}$ and $R\overline{3}$. Error bars are shown, if not visible, they are the size of the symbol or below. Legend of the figure provides additional information on PTMs used in individual loadings.

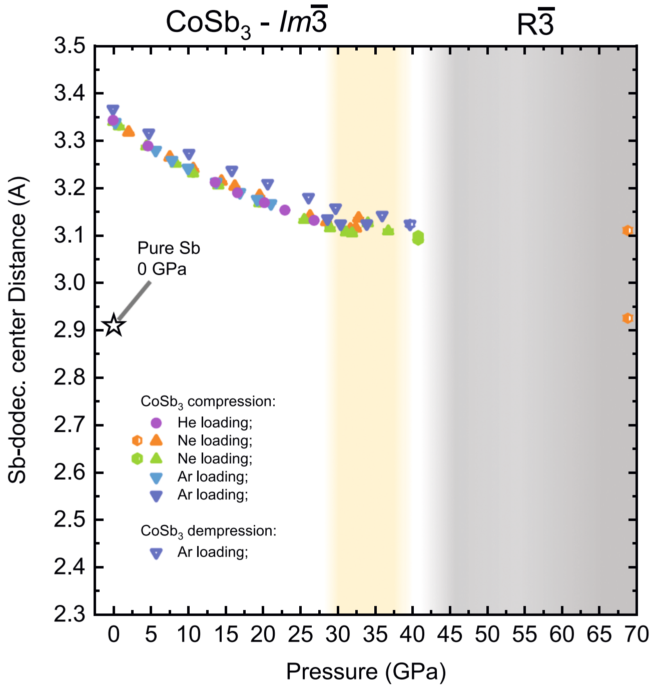

Fig. 10. Distance between a center of a dodecahedral cite (2a Wyckoff site of $Im\overline{3}$ or a compatible site in $R\overline{3}$) to the next nearest neighbor represented by other Sb atoms. We indicate the Sb-Sb distance corresponding to pure antimony at ambient conditions using the star symbol [46,47]. We highlight the region of the 'self-insertion' using the yellow shading and the stability field of $R\overline{3}$ using grey shading. Solid circles and triangles correspond to the cubic $Im\overline{3}$ phase. The orange hexagons correspond to the trigonal $R\overline{3}$ phase. For the reader's convenience, we present values calculated for both $Im\overline{3}$ and $R\overline{3}$ for the selected pressure of ~40 GPa. Error bars are shown, if not visible, they are the size of the symbol or below. Legend of the figure provides additional information on PTMs used in individual loadings.

occupying the dodecahedral sites with its closest neighbors should be non-covalent even at pressures as high as 70 GPa, namely within the $R\overline{3}$ phase's stability field.

In order to fill all dodecahedral sites of the $Im\overline{3}$ phase, one requires only two Sb vacancies per unit cell with the vacancies formed at the cost of Sb surrounding the Co atoms. According to our observations, in the vicinity of the 'self-insertion' crossover, the diffusion triggered by the process covers large atomic distances, and it happens fast – on the order of seconds or much less, depending on the pressure step. We observe that collective 'mass transport' correlated with random redistribution of Sb atom driven by the 'self-insertion' occurs under conditions where ambient temperature kinetics are strongly suppressed. This features the unique underlying nature of the process.

We suggest that for a more accurate characterization of the system we need to extend theoretical picture of $CoSb_3$. It is known that at ambient conditions the material in the $Im\overline{3}$ structure should be a small direct bandgap semiconductor [53]. Under compression, but prior to 'self-insertion', the $CoSb_3$ bandgap may become indirect and an experiment shows that resistivity increases with compression [54]. We have to admit that the picture is complex, and it is far from being complete. Thorough theoretical investigations of the material with 'self-insertion' induced atomic disorder of Sb atoms are still missing, but they may generalize the picture of strongly correlated $CoSb_3$ and the phenomenon of 'self-insertion' in comparison with other skutterudite materials. The formation of the $R\overline{3}$ phase inheriting the Sb atomic disorder adds another layer of complexity and should also be addressed by theory.

From a crystallographic point of view, the $Im\overline{3} \rightarrow R\overline{3}$ phase transition follows a group-subgroup path, and in Fig. 11 we show the relation between both structures at 40.8(2) GPa, which corresponds to the end of 'self-insertion' crossover. A diagram capturing the relation can be found in the Ch. 4 of Supplementary [20]. In Fig. 11, we indicate the disorder in the occupancy of different atomic Sb positions and highlight the occupied dodecahedral sites using the black color. The unit cell of the $R\overline{3}$ phase is larger ($Z = 12$) than that of the $Im\overline{3}$ phase ($Z = 8$). The compression-induced symmetry decrease results in the formation of additional independent Co and Sb sites. In the $R\overline{3}$ phase, the Wyckoff symbols for the $CoSb_6$ octahedra forming Co are 3*b* and 9*d*, and for Sb it is 18 *f*. The Sb atoms occupying dodecahedral sites have the Wyckoff symbol 3*a*.

As one can see from Fig. 4 and Fig. 11, at ~40.8(2) GPa the Sb occupancies in the dodecahedral sites are slightly below 100 %. We also observe that the corresponding Sb occupancies of the $CoSb_6$ octahedra are high, with values of 94 %. As mentioned above, due to limited synchrotron beamtime access, we could only measure reliably the $R\overline{3}$ crystal structure for the pressure of 68.8(2) GPa. Although the resulting *R1* factor is not as low as for lower pressures (e.g. enlisted in the Ch. 7, tables of Supplementary [20]), because the atomic disorder caused diffraction peak broadening and a decrease in the signal-to-noise ratio at high 2θ°, we consider the major observations as being valid. In Fig. 12 we compare the crystal structure modification of the $R\overline{3}$ phase by compression, showing different structural projections side by side.

Complementary to Fig. 9, in Fig. 12 we show the shortest Sb-Sb bond distances by means of green cylinders interconnecting green atoms. Although the bonds shrink as a result of compression, these structural elements remain unchanged through the whole compression range which supports the predominantly covalent nature of these Sb-Sb bonds. The dodecahedral sites become fully filled by Sb atoms at 68.8(2) GPa, however, it is not the most striking feature. In comparison to the pressure 40.8(2) GPa, we see a stronger distortion of the light blue octahedrons in comparison to the pink ones. Both type of octahedra can be described as $CoSb_{6\text{-}\Delta}$ with Δ denoting vacancies at the Sb sites surrounding Co. The distortion does not result in a strong change of octahedra volume, as we show in Ch. 6 of Supplementary [20]. Still, it is clear that the crystal fields of Co occupying the pink and the light blue octahedrons should be different. This observation is supporting our hypothesis of a compression-induced impactful modification of electronic properties. We note that the light blue octahedra interconnect the fully occupied dodecahedral sites, and together they form channels along the *c*-axis of the $R\overline{3}$ phase.

As previously mentioned, $CoSb_3$ exhibits a behavior that is in stark contrast to many other known strongly correlated materials. In particular, it should become more insulating under stress [54] while many other materials show the opposite behavior [55,56]. It may be that the structural transformation to the phase and the evolution of its crystal chemistry promotes the metallization of the compound; however, in order to solve this and other challenges behind the physics of $CoSb_3$ (in particular) and of skutterudite materials (in general), crystallographic experimental data are not enough. We require advancements in the field of theoretical calculations, particularly for materials with structural disorder, which remain challenging and complex and are beyond the scope of this study.

4. Conclusions

Our paper addresses one of the most famous unfilled skutterudite material, $CoSb_3$, used as a platform for thermoelectric applications. Beyond thermoelectrics, it also provides an excellent example of strong correlations under compression which were previously under-characterized. Complementary to previous studies, we present a great amount of data collected on single crystalline material with a focus on the particular 'self-insertion' crossover. This crossover is attributed to a reduced, or as we show in our data potentially even negative, compressibility. By presenting data collected from small crystallites

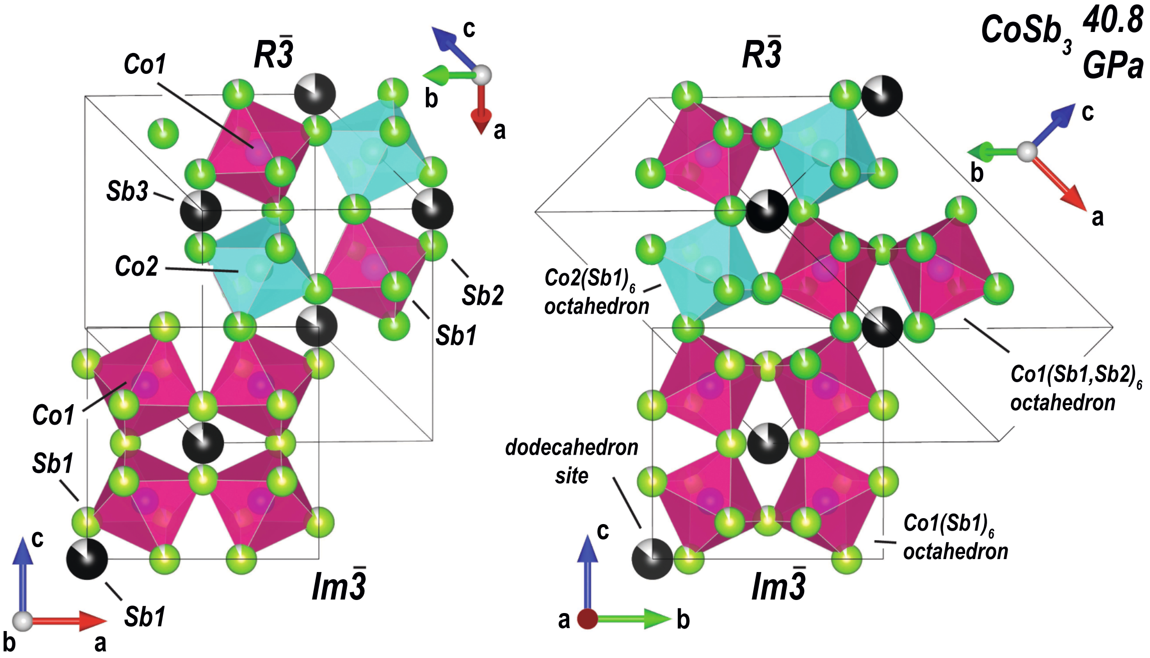

Fig. 11. Comparison between the lower pressure $Im\overline{3}$ and the higher pressure $R\overline{3}$ structures using 40.8(2) GPa as a reference point. The corresponding crystallographic R1 factors for $Im\overline{3}$ and $R\overline{3}$ are R1 = 6.64 % and R1 = 6.85 %, respectively. The crystallographic R-factors correspond to $I > 2\sigma(I)$ with I and σ being attributed to the measured intensities and their standard deviations, respectfully. The left and the right panels demonstrate different projections at the same structures. The vectors forming the corresponding unit cells are shown in each panel in the lower left corner for $Im\overline{3}$ and in the upper right corner for $R\overline{3}$, respectfully. The lattice parameters a and b of $R\overline{3}$ lie within a plane perpendicular to [111] of $Im\overline{3}$. By using the black color, we highlight the Sb atoms populating dodecahedral sites and by green – the Sb atoms being part of $CoSb_6$ octahedrons. Occupational disorder of Sb atoms is indicated. Comparing the structures, we observe an addition of independent atomic positions of Co and Sb forming $CoSb_6$ octahedrons in $R\overline{3}$ (e.g. the octahedra painted in light blue and pink).

surrounded by different PTMs, we discuss various effects, including the extreme sensitivity of $CoSb_3$ to external stress and strain conditions. Among other results, we show that the 'self-insertion' crossover may happen at different stress (e.g. HSC vs SCS), but also at different average strain, namely different unit cell volumes (e.g. Ne vs Ar PTM loadings). These findings should be carefully considered for other skutterudite materials, including $RhSb_3$ and $IrSb_3$, both reported by Matsui et al. [15], and others. In most of conventional high-pressure experiments, the important details of realistic sample loadings with their stresses and strains are only briefly discussed. As we demonstrate here, in strongly correlated systems like $CoSb_3$, these factors play a significant role and should not be neglected. This is important not only for theoretical studies but also for benchmarking experimental data and vice versa.

The results collected below 70 GPa allow us to reference the 'self-insertion' crossover as an intermediate isostructural transition of $CoSb_3$ $Im\overline{3}$ preceding the transformation into the novel $R\overline{3}$ phase. Although, $CoSb_3$ was compressed to pressures of 40 GPa and slightly above previously [15], the transformation into $R\overline{3}$ has not been found before. This is most probably due to the effects of large inter-grain strain and disorder within the studied powder material resulting in the inability to resolve diffraction peak splitting. We can also mention that powder data would not allow reliable indexing and structure solution, which, to the best of our knowledge, is presented for the $R\overline{3}$ phase for the first time.

In our study, we also discuss progress within our understanding of the electronic properties of $CoSb_3$ and emphasize that there are many missing puzzle pieces. Our experimental results describe the intriguing crystal chemistry of $CoSb_3$ and its evolution under pressure and indicate a potential for readjustment of electronic properties as a result of compression. They present a great benchmark data for future calculations involving atomic disorder. We hope that our work will inspire more precise and accurate theoretical models, shedding light on complex electron correlation phenomena natural not only in $CoSb_3$, but also in the general family of unfilled skutterudites.

CRediT authorship contribution statement

Ren Zhe: Writing – review & editing, Writing – original draft, Visualization, Software, Methodology, Formal analysis, Data curation. **Gille Peter:** Writing – review & editing, Writing – original draft, Resources, Methodology, Investigation, Funding acquisition, Formal analysis, Data curation. **Glazyrin Konstantin:** Writing – review & editing, Writing – original draft, Visualization, Validation, Supervision, Software, Resources, Project administration, Methodology, Investigation, Funding acquisition, Formal analysis, Data curation, Conceptualization. **Assalauova Dameli:** Writing – review & editing, Writing – original draft, Visualization, Resources, Formal analysis, Data curation. **Lapkin Dmitry:** Writing – review & editing, Writing – original draft, Visualization, Software, Resources, Methodology, Formal analysis. **Alexeev Pavel:** Writing – review & editing, Writing – original draft, Methodology, Investigation. **Kulkarni Satishkumar:** Writing – review & editing, Writing – original draft, Resources, Methodology, Investigation, Formal analysis. **Sergeev Ilya:** Writing – review & editing, Writing – original draft, Visualization, Methodology, Investigation, Funding acquisition, Conceptualization. **Pakhomova Anna:** Writing – review & editing, Writing – original draft, Visualization, Resources, Methodology, Investigation, Formal analysis, Data curation. **Sprung Michael:** Writing – review & editing, Writing – original draft, Visualization, Resources, Methodology, Investigation. **Wang Bihan:** Writing – review & editing, Writing – original draft, Visualization, Validation, Software, Resources, Methodology, Investigation, Formal analysis, Data curation. **Weng Tsu-Chien:** Writing – review & editing, Writing – original draft, Resources, Funding acquisition. **Pillaca Mirtha:** Writing – review & editing, Writing – original draft, Resources, Methodology, Investigation, Formal analysis, Data curation. **Vartanyants Ivan A.:** Writing – review & editing, Writing – original draft, Visualization, Validation, Supervision, Software, Resources, Project administration, Methodology, Investigation, Funding acquisition, Formal analysis, Data curation,

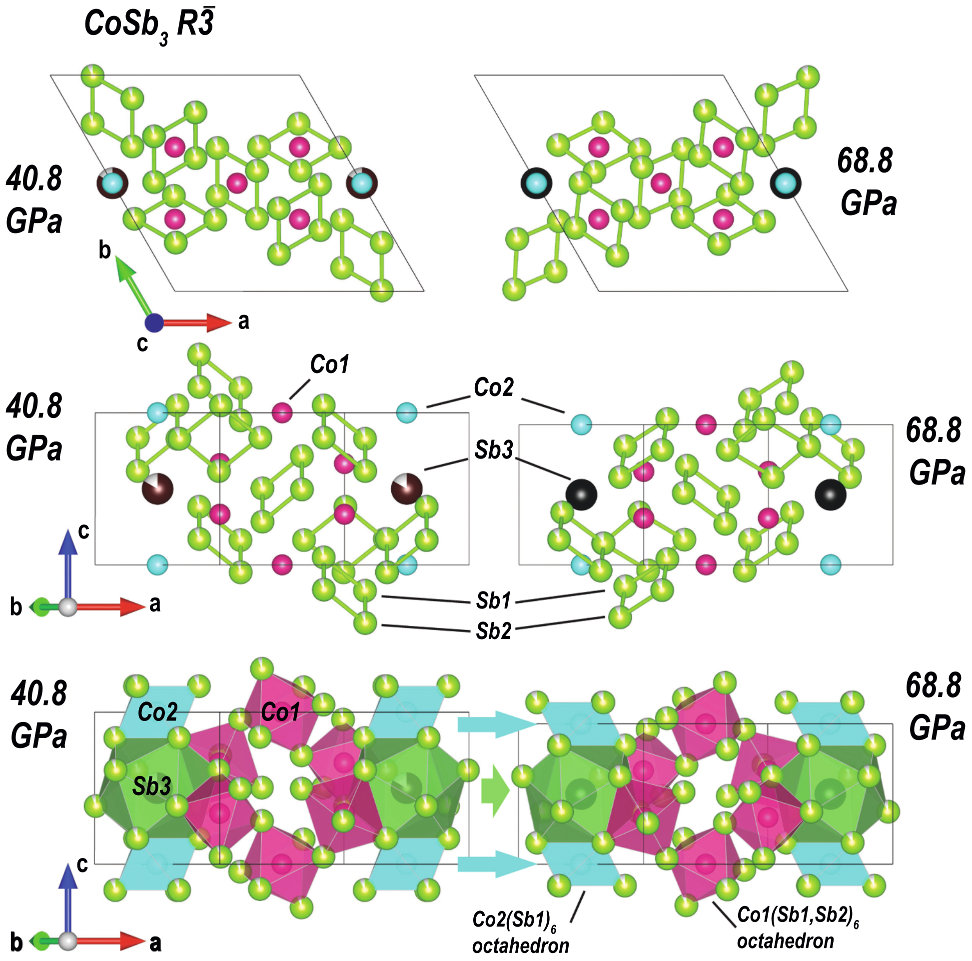

Fig. 12. Illustration of R$\overline{3}$ phase compression driven changes. We compare data for structures solved at 40.8(2) and at 68.8(2) GPa. Individual crystallographic sites are indicated together with the unit cell vectors for each of the projections. By black color we indicate the Sb atoms populating the dodecahedral sites. Note the full occupancy of these sites at the 68.8(2) GPa. The structural solution at the highest pressure has the R-factor R1 = 10.5 %. Using solid green cylinders, we indicate the shortest Sb-Sb bond distances (see also Fig. 9). The most striking feature is the distortion of Co2(Sb1)$_6$ light blue octahedra squashed between dodecahedral sites along c-axis of R$\overline{3}$. The dark green dodecahedral sites together with the light blue octahedra form vertical channels. In comparison to the light blue ones, the pink octahedra remain less distorted.

Conceptualization. **Khandarkhaeva Saiana:** Writing – review & editing, Writing – original draft, Visualization, Resources, Methodology, Investigation, Formal analysis, Data curation, Conceptualization. **Liermann Hanns-Peter:** Writing – review & editing, Writing – original draft, Supervision, Resources, Project administration, Investigation, Funding acquisition, Formal analysis, Conceptualization.

Declaration of Competing Interest

The authors declare that they have no known competing financial interests or personal relationships that could have appeared to influence the work reported in this paper

Acknowledgements

We acknowledge DESY (Hamburg, Germany), a member of the Helmholtz Association HGF, for the provision of experimental facilities. Parts of this research were carried out at P02.2 beamline of PETRA III and DESY NanoLab. We would like to thank Thomas F. Keller for assistance in using DESY NanoLab FIB machine. The FIB milling capability was provided via a „Bundesministerium für Bildung und Forschung“ grant under contract 05K12WC1 and 05K16WC1 in the framework of the Verbundforschung “Einkristallkristallographie bei hohem Druck und variabler Temperatur” (PI.: Prof. Dr. N. Dubrovinskaia, Uni. Bayreuth). B.W. acknowledges funding provided by Office of the China Postdoctoral Council (OCPC) of the Chinese Ministry of Human Resources and Social Security (MoHRSS) within Helmholtz-OCPC program. We thank anonymous reviewers for their help to improve the manuscript. We gratefully acknowledge Dr. Dominique Laniel for his valuable time and effort in reading and providing critical feedback on this manuscript, which significantly improved its clarity and presentation.

Appendix A. Supporting information

Supplementary data associated with this article can be found in the online version at doi:10.1016/j.jallcom.2025.179020.

Data availability

Data will be made available on request.

References

[1] H. Rakoto, E. Arushanov, M. Respaud, J.M. Broto, J. Leotin, C. Kloc, E. Bucher, S. Askenazy, Shubnikov–de Haas Oscillations in CoSb$_3$ Single crystals under high magnetic fields, Phys. B Condens. Matter 246-247 (1998) 528, https://doi.org/10.1016/S0921-4526(97)00978-2.

[2] D.T. Morelli, T. Caillat, J.P. Fleurial, A. Borshchevsky, J. Vandersande, B. Chen, C. Uher, Low-temperature transport properties of p-Type CoSb$_3$, Phys. Rev. B 51 (1995) 9622, https://doi.org/10.1103/physrevb.51.9622.

[3] J.E.F.S. Rodrigues, J. Gainza, F. Serrano-Sánchez, C. Marini, Y. Huttel, N. M. Nemes, J.L. Martínez, J.A. Alonso, Atomic structure and lattice dynamics of CoSb$_3$ skutterudite-based thermoelectrics, Chem. Mater. 34 (2022) 1213, https://doi.org/10.1021/acs.chemmater.1c03747.

[4] T. Dahal, Q. Jie, G. Joshi, S. Chen, C. Guo, Y. Lan, Z. Ren, Thermoelectric property enhancement in yb-doped n-type skutterudites Yb$_x$Co$_4$Sb$_{12}$, Acta Mater. 75 (2014) 316, https://doi.org/10.1016/j.actamat.2014.05.019.

[5] Z.Y. Liu, J.L. Zhu, X. Tong, S. Niu, W.Y. Zhao, A review of CoSb$_3$-based skutterudite thermoelectric materials, J. Adv. Ceram. 9 (2020) 647, https://doi.org/10.1007/s40145-020-0407-4.

[6] T. Caillat, A. Borshchevsky, J.P. Fleurial, Properties of single crystalline semiconducting CoSb$_3$, J. Appl. Phys. 80 (1996) 4442, https://doi.org/10.1063/1.363405.

[7] Y. Tang, Z.M. Gibbs, L.A. Agapito, G. Li, H.S. Kim, M.B. Nardelli, S. Curtarolo, G. J. Snyder, Convergence of multi-valley bands as the electronic origin of high thermoelectric performance in CoSb$_3$ skutterudites, Nat. Mater. 14 (2015) 1223, https://doi.org/10.1038/nmat4430.

[8] S. Li, X. Jia, H. Ma, First-principles investigation of electronic structure and transport properties of CoSb$_3$ under different pressures, Chem. Phys. Lett. 549 (2012) 22, https://doi.org/10.1016/j.cplett.2012.08.006.

[9] X. Pang, M. He, F. Zhang, B. Jia, W. Wang, X. Cao, M. Song, X. Chao, Z. Yang, D. Wu, Ultrahigh thermoelectric power factor achieved in Yb filled CoSb$_3$ skutterudites through additional Al doping, Chem. Eng. J. 481 (2024) 148457, https://doi.org/10.1016/j.cej.2023.148457.

[10] D. Li, X.-L. Shi, J. Zhu, T. Cao, X. Ma, M. Li, Z. Han, Z. Feng, Y. Chen, J. Wang, W.-D. Liu, H. Zhong, S. Li, Z.-G. Chen, High-performance flexible p-type Ce-filled Fe$_3$CoSb$_{12}$ skutterudite thin film for medium-to-high-temperature applications, Nat. Commun. 15 (2024) 4242, https://doi.org/10.1038/s41467-024-48677-4.

[11] A.C. Kraemer, M.R. Gallas, J.A.H. Da Jornada, C.A. Perottoni, Pressure-induced self-insertion reaction in CoSb$_3$, Phys. Rev. B 75 (2007) 024105, https://doi.org/10.1103/PhysRevB.75.024105.

[12] X. Li, Q. Zhang, Y. Kang, C. Chen, L. Zhang, D. Yu, Y. Tian, B. Xu, High-pressure synthesized Ca-filled CoSb$_3$ skutterudites with enhanced thermoelectric properties, J. Alloy. Compd. 677 (2016) 61, https://doi.org/10.1016/j.jallcom.2016.03.239.

[13] F. Miotto, C.A. Figueirêdo, G.R. Ramos, C.L.G. Amorim, M.R. Gallas, C. A. Perottoni, Antimony desinsertion reaction from Sb$_x$CoSb$_{3\text{-}x}$, J. Appl. Phys. 110 (2011), https://doi.org/10.1063/1.3626045.

[14] R. Viennois, T. Kume, M. Komura, L. Girard, A. Haidoux, J. Rouquette, M.M. Koza, Raman-scattering experiments on unfilled skutterudite CoSb$_3$ under high pressure and high temperature, J. Phys. Chem. C. 124 (2020) 23004, https://doi.org/10.1021/acs.jpcc.0c06703.

[15] K. Matsui, J. Hayashi, K. Akahira, K. Ito, K. Takeda, C. Sekine, Pressure-induced irreversible isosymmetric transition of TSb$_3$ (T=Co, Rh and Ir), J. Phys. Conf. Ser. 215 (2010) 012005, https://doi.org/10.1088/1742-6596/215/1/012005.

[16] Y. Kang, F. Yu, C. Chen, Q. Zhang, H. Sun, L. Zhang, D. Yu, Y. Tian, B. Xu, High pressure synthesis and thermoelectric properties of Ba-filled CoSb$_3$ skutterudites, J. Mater. Sci. Mater. Electron. 28 (2017) 8771, https://doi.org/10.1007/s10854-017-6603-5.

[17] K. Awaji, K. Nishimura, K. Suwa, J. ichi Hayashi, Y. Kawamura, K. Takeda, H. Gotou, C. Sekine, Significant changes in thermoelectric properties of unfilled skutterudite compounds MSb$_3$ (M = Co and Rh) by self-insertion reaction, Mater. Today Commun. 36 (2023) 106825, https://doi.org/10.1016/j.mtcomm.2023.106825.

[18] K. Glazyrin, N. Miyajima, J.S. Smith, K.K.M. Lee, Compression of a multiphase mantle assemblage: effects of undesirable stress and stress annealing on the iron spin state crossover in ferropericlase, J. Geophys. Res. Solid Earth 121 (2016) 3377, https://doi.org/10.1002/2015JB012321.

[19] W. Xu, W. Dong, S. Layek, M. Shulman, K. Glazyrin, E. Bykova, M. Bykov, M. Hanfland, M.P. Pasternak, I. Leonov, E. Greenberg, G.Kh Rozenberg, Pressure-induced high-spin/low-spin disproportionated state in the Mott insulator FeBO$_3$, Sci. Rep. 12 (2022) 9647, https://doi.org/10.1038/s41598-022-13507-4.

[20] Supplementary data associated with this article can be found in the online version at doi:10.1016/j.jallcom.2025.179020. Supplementary information shows additional experimental detail. CIF files are also submitted as a part of Supplementary.

[21] J. Miao, T. Ishikawa, I.K. Robinson, M.M. Murnane, Beyond crystallography: diffractive imaging using coherent x-ray light sources, Science 348 (2015) 530, https://doi.org/10.1126/science.aaa1394.

[22] I.K. Robinson, I.A. Vartanyants, G.J. Williams, M.A. Pfeifer, J.A. Pitney, Reconstruction of the shapes of gold nanocrystals using coherent x-ray diffraction, Phys. Rev. Lett. 87 (2001) 195505, https://doi.org/10.1103/PhysRevLett.87.195505.

[23] M.A. Pfeifer, G.J. Williams, I.A. Vartanyants, R. Harder, I.K. Robinson, Three-dimensional mapping of a deformation field inside a nanocrystal, Nature 442 (2006) 63, https://doi.org/10.1038/nature04867.

[24] W. Yang, X. Huang, R. Harder, J.N. Clark, I.K. Robinson, H.K. Mao, Coherent diffraction imaging of nanoscale strain evolution in a single crystal under high pressure, Nat. Commun. 4 (2013) 1680, https://doi.org/10.1038/ncomms2661.

[25] I. Robinson, R. Harder, Coherent x-ray diffraction imaging of strain at the nanoscale, Nat. Mater. 8 (2009) 291, https://doi.org/10.1038/nmat2400.

[26] K. Glazyrin, S. Khandarkhaeva, T. Fedotenko, W. Dong, D. Laniel, F. Seiboth, A. Schropp, J. Garrevoet, D. Brückner, G. Falkenberg, A. Kubec, C. David, M. Wendt, S. Wenz, L. Dubrovinsky, N. Dubrovinskaia, H.P. Liermann, Sub-micrometer focusing setup for high-pressure crystallography at the extreme conditions beamline at PETRA III, J. Synchrotron Radiat. 29 (2022) 654, https://doi.org/10.1107/s1600577522002582.

[27] M. Pillaca, O. Harder, W. Miller, P. Gille, Forced convection by inclined rotary Bridgman method for growth of CoSb$_3$ and FeSb$_2$ single crystals from Sb-rich solutions, J. Cryst. Growth 475 (2017) 346, https://doi.org/10.1016/j.jcrysgro.2017.07.016.

[28] R. Boehler, K. De Hantsetters, New anvil designs in diamond-cells, High. Press. Res. 24 (2004) 391, https://doi.org/10.1080/08957950412331323924.

[29] I. Kantor, V. Prakapenka, A. Kantor, P. Dera, A. Kurnosov, S. Sinogeikin, N. Dubrovinskaia, L. Dubrovinsky, BX90: a new diamond anvil cell design for x-ray diffraction and optical measurements, Rev. Sci. Instrum. 83 (2012) 125102, https://doi.org/10.1063/1.4768541.

[30] A. Dewaele, M. Torrent, P. Loubeyre, M. Mezouar, Compression curves of transition metals in the Mbar range: experiments and projector augmented-wave calculations, Phys. Rev. B 78 (2008) 104102, https://doi.org/10.1103/physrevb.78.104102.

[31] Y. Fei, A. Ricolleau, M. Frank, K. Mibe, G. Shen, V. Prakapenka, Toward an Internally Consistent Pressure Scale, PNAS 104 (2007) 9182, https://doi.org/10.1073/pnas.0609013104.

[32] A. Dewaele, A.D. Rosa, N. Guignot, D. Andrault, J.E.F.S. Rodrigues, G. Garbarino, Stability and equation of state of face-centered cubic and hexagonal close packed phases of argon under pressure, Sci. Rep. 11 (2021) 15192, https://doi.org/10.1038/s41598-021-93995-y.

[33] H.-P. Liermann, Z. Konôpková, W. Morgenroth, K. Glazyrin, J. Bednarčik, E. E. McBride, S. Petitgirard, J.T. Delitz, M. Wendt, Y. Bican, A. Ehnes, I. Schwark, A. Rothkirch, M. Tischer, J. Heuer, H. Schulte-Schrepping, T. Kracht, H. Franz, The Extreme Conditions Beamline P02.2 and the Extreme Conditions Science Infrastructure at PETRA, III, J. Synchrotron Radiat. 22 (2015) 908, https://doi.org/10.1107/S1600577515005937.

[34] C. Prescher, V.B. Prakapenka, DIOPTAS: a program for reduction of two-dimensional x-ray diffraction data and data exploration, High. Press. Res. 35 (2015) 223, https://doi.org/10.1080/08957959.2015.1059835.

[35] Rigaku Crysalis Pro v. 171.40, CrysAlis PRO software package.

[36] V. Petricek, M. Dusek, L. Palatinus, Crystallographic computing system JANA2006: General features, Z. Krist. 229 (5) (2014) 345–352, https://doi.org/10.1515/zkri-2014-1737.

[37] O.V. Dolomanov, L.J. Bourhis, R.J. Gildea, J.A.K. Howard, H. Puschmann, OLEX2: a complete structure solution, refinement and analysis program, J. Appl. Cryst. 42 (2009) 339, https://doi.org/10.1107/S0021889808042726.

[38] G.M. Sheldrick, A Short History of SHELX, Acta Cryst. A 64 (2008) 112, https://doi.org/10.1107/S0108767307043930.

[39] P. Müller, Crystal Structure Refinement: A Crystallographers Guide to SHELXL, Oxford University Press, 2006. ISBN: 9780198570769), https://doi.org/10.1093/acprof:oso/9780198570769.001.0001.

[40] K. Momma, F. Izumi, VESTA 3 for three-dimensional visualization of crystal, volumetric and morphology data, J. Appl. Cryst. 44 (2011) 1272, https://doi.org/10.1107/S0021889811038970.

[41] D.C. Palmer, CrystalMaker X, 10.8.1 software package.

[42] H. Xu, Z. Ren, M. Sprung, PyCXIM: Python Scr. Coherent X-Ray Imaging Methods (2024) https://github.com/RenZhe88/pyCXIM.

[43] S. Marchesini, H. He, N. Chapman, P. Hau-Riege, A. Noy, R. Howells, U. Weierstall, H. Spence, X-ray image reconstruction from a diffraction pattern alone, Phys. Rev. B 68 (2003) 140101R, https://doi.org/10.1103/Phys. RevB.68.140101.

[44] T. Rosenqvist, Magnetic and crystallographic studies on the higher antimonies of iron, cobalt and nickel, Acta Met. 1 (1953) 761.

[45] S. Klotz, J.C. Chervin, P. Munsch, G. Le Marchand, Hydrostatic limits of 11 pressure transmitting media, J. Phys. D: Appl. Phys. 42 (2009) 075413, https://doi.org/10.1088/0022-3727/42/7/075413.

[46] J.Q. Li, X.W. Feng, W.A. Sun, W.Q. Ao, F.S. Liu, Y. Du, Solvothermal synthesis of nano-sized skutterudite Co$_{4-x}$Fe$_x$Sb$_{12}$ powders, Mater. Chem. Phys. 112 (2008) 57, https://doi.org/10.1016/j.matchemphys.2008.05.017.

[47] C.S. Barrett, P. Cucka, K. Haefner, The crystal structure of antimony at 4.2, 78 and 298° K, Acta Cryst. 16 (1963) 451, https://doi.org/10.1107/S0365110X63001262.

[48] D. Schiferl, and D. Schiferlt, 50-kilobar gasketed diamond anvil cell for single-crystal x-ray diffractometer use with the crystal structure of sb up to 26 kilobars as a test problem, Rev. Sci. Instrum. 48 (1977) 24, https://doi.org/10.1063/1.1134861.

[49] D. Schiferl, D.T. Cromer, J.C. Jamieson, Structure determinations on Sb up to 85 x 10^2 MPa, Acta Cryst. B 37 (1981) 807, https://doi.org/10.1107/S0567740881004378.

[50] U. Schwarz, L. Akselrud, H. Rosner, A. Ormeci, Y. Grin, M. Hanfland, Structure and stability of the modulated phase Sb-II, Phys. Rev. B 67 (2003) 214101, https://doi.org/10.1103/PhysRevB.67.214101.

[51] O. Degtyareva, M.I. Mcmahon, R.J. Nelmes, High-Pressure structural studies of Group-15 Elements, High. Press. Res. 24 (2004) 319, https://doi.org/10.1080/08957950412331281057.

[52] S. Lee, H. Xu, H. Xu, J. Neuefeind, Crystal structure of moganite and its anisotropic atomic displacement parameters determined by synchrotron x-ray diffraction and x-ray/neutron pair distribution function analyses, Minerals 11 (2021) 272, https://doi.org/10.3390/min11030272.

[53] L. Hammerschmidt, S. Schlecht, B. Paulus, Electronic structure and the ground-state properties of cobalt antimonide skutterudites: revisited with different theoretical methods, Phys. Status Solidi A (2013) 131, https://doi.org/10.1002/pssa.201228453.

[54] L. Wu, Y. Sun, G.Z. Zhang, C.X. Gao, Pressure-induced improvement of Seebeck coefficient and thermoelectric efficiency of $CoSb_3$, Mater. Lett. 129 (2014) 68, https://doi.org/10.1016/j.matlet.2014.04.095.

[55] V.V. Brazhkin, D.R. Dmitriev, R.N. Voloshin, Metallization of Mg_3Bi_2 under pressure in crystalline and liquid state, Phys. Lett. A 193 (1994) 102, https://doi.org/10.1016/0375-9601(94)00603-2.

[56] C.W. Nicholson, F. Petocchi, B. Salzmann, C. Witteveen, M. Rumo, G. Kremer, O. Ivashko, F.O. Von Rohr, P. Werner, C. Monney, Gap collapse and flat band induced by uniaxial strain in 1T-TaS_2, Phys. Rev. B 109 (2024) 035167, https://doi.org/10.1103/PhysRevB.109.035167.